International Journal of Solids and Structures 45 (2008) 6018–6033

Contents lists available at ScienceDirect

International Journal of Solids and Structures

journal homepage: www.elsevier.com/locate/ijsolstr

An analysis of nanoindentation in linearly elastic solids

B. Poon [a], D. Rittel [b], G. Ravichandran [a,*]

[a] Graduate Aeronautical Laboratories, California Institute of Technology – Pasadena, Pasadena, CA 91125, USA
[b] Faculty of Mechanical Engineering, Technion, 32000 Haifa, Israel

ARTICLE INFO

Article history:
Received 1 April 2008
Received in revised form 29 May 2008
Available online 6 August 2008

Keywords:
Indentation
Elastic solids
Elastic modulus
Mechanics
Finite elements

ABSTRACT

The conventional method to extract elastic properties in the nanoindentation of linearly elastic solids relies primarily on Sneddon's solution (1948). The underlying assumptions behind Sneddon's derivation, namely, (1) an infinitely large incompressible specimen; (2) an infinitely sharp indenter tip, are generally violated in nanoindentation. As such, correction factors are commonly introduced to achieve accurate measurements. However, little is known regarding the relationship between the correction factors and how they affect the overall accuracy. This paper first proposes a criterion for the specimen's geometry to comply with the first assumption, and modifies Sneddon's elastic relation to account for the finite tip radius effect. The relationship between the finite tip radius and compressibility of the specimen is then examined and a composite correction factor that involves both factors, derived. The correction factor is found to be a function of indentation depth and a critical depth is derived beyond which, the arbitrary finite tip radius effect is insignificant. Techniques to identify the radius of curvature of the indenter and to decouple the elastic constants (E and ν) for linear elastic materials are proposed. Finally, experimental results on nanoindentation of natural latex are reported and discussed in light of the proposed modified relation and techniques.

1. Introduction

Nanoindentation has become an increasingly popular mechanical characterization technique in the last decade. In addition to measuring the hardness value, the depth-sensing indentation has been routinely used to extract the elastic properties of the specimen, with known indenter geometry and material properties. Nanoindentation was developed in the early 1970s (Bulychev et al., 1975; Loubet et al., 1984; Newey et al., 1982; Pethica et al., 1983; Ternovskii et al., 1974). The technological developments have reduced the size of tips manufactured, and improved the accuracy and resolution of depth and load measurement of the indentation test, which has spurred the development of commercial nanoindenters. Their popularity is primarily due to the increased interest in thin films and specimens with small volumes as motivated by modern applications, e.g., thin films, microelectronics, MEMS, biomaterials etc. In addition, nano characterization instruments such as the atomic force microscope (AFM) are being widely used for performing nanoindentation on a wide range of materials (e.g., Bhushan and Koinkar, 1994; Dimitriadis et al., 2002; VanLandingham et al., 2001). When compared to other methods of mechanical testing in the sub-micron range, nanoindentation has a relatively simple setup and specimen preparation. Furthermore, nanoindentation leaves a small imprint and is commonly perceived as relatively non-destructive.

The indentation problem has been studied for over a century, beginning with Hertz's pioneering contribution on the contact between elastic bodies (Hertz, 1881). Boussinesq (1885) subsequently studied the contact problem between two linearly elastic isotropic solids using methods of potential theory, which proved to be a significant milestone to the understanding of

* Corresponding author. Tel.: +1 626 395 4525; fax: +1 626 449 6359.
E-mail address: ravi@caltech.edu (G. Ravichandran).

0020-7683/$ - see front matter © 2008 Elsevier Ltd. All rights reserved.
doi:10.1016/j.ijsolstr.2008.07.021

the indentation problem. Sneddon used the approach taken by Bousinnesq to derive the load–displacement relationship for a rigid cone indenter (1948), and subsequently derived it for an arbitrary indenter that is a body of revolution (1965). However, the analytical solutions were derived with stringent assumptions – (1) the specimen is an infinite half-space, (2) the indenter has an ideal geometry with known parameters (perfect cone, sphere, etc.), and (3) the material is linearly elastic and incompressible. These assumptions limit the application of these solutions to many problems of practical interest. However, with the advent of finite element simulations and commercial codes, researchers now have a new tool to investigate the indentation problem, e.g., on spherical indenter – Hill et al. (1989), Kral et al. (1993), and Storåkers and Larsson (1994); on conical indenter – Laursen and Simo (1992); on pyramidal indenters – Giannakopoulos et al. (1994) and Larsson and Giannakopoulos (1996); on effects of plasticity, Pharr et al. (1992) and Cheng and Cheng (1999); and on forward–reverse analysis in nanoindentation, Dao et al. (2001) and Chen et al. (2007).

Pyramidal indenters (three-sided Berkovich and four-sided Vickers) are commonly used in indentation tests. These indenters are commonly treated as conical indenters with equivalent half-angle α that gives the same area to depth relationship as the pyramidal indenter in question (Fischer-Cripps, 2004; Lichinchi et al., 1998; Oliver and Pharr, 1992; Wang et al., 2006; Yu et al., 2004).

The conventional procedure to derive the elastic properties during an indentation experiment was first proposed by Oliver and Pharr (1992), who made use of Sneddon's solution to retrieve the reduced modulus, E_r. Due to the stringent assumptions made in Sneddon's theoretical derivation as discussed previously, a correction factor is introduced to achieve accurate results. The correction factor is commonly derived using two approaches, (1) phenomenological approach and (2) mechanistic approach. Using the phenomenological approach, researchers often establish a composite correction factor by comparing the macroscopic material properties obtained using traditional characterization techniques such as uniaxial test, with that obtained using nanoindentation for different classes of materials such as polymers, metals and ceramics, etc. (Tranchida et al., 2006). This composite correction factor obtained takes into account all the factors that violates the assumptions in the theoretical derivations, however, this approach does not provide insight to the makeup of the correction factor by different factors, nor does it show how the factors affect one another. For the mechanistic approach, researchers often isolate one individual factor not considered in the theoretical derivation. Using this approach, researchers are able to gain tremendous insight about this isolated factor, for example, in the compressibility of the specimen when $\nu < 0.5$, which results in a lateral displacement during indentation, neglected in Sneddon's derivation (Hay et al., 1999), researchers were able to derive a close form expression for the correction factor that relates to the Poisson's ratio, ν. However, it is often not clear if this correction factor is applicable to practical indentations that commonly involve other factors as well, i.e. can this factor derived using linear elastic conditions be used in elastic–plastic indentations? And, how do different correction factors relate to each other to form the effective correction factor for the nanoindentation experiment?

This paper first critically examines the various assumptions used in extracting the linearly elastic material properties using numerical finite element calculations, and identifies the sources of deviation from theoretical assumptions including the finite tip radius and the lateral displacement at the indentation. The conventional procedure for extracting the reduced modulus is briefly reviewed in Section 2. Results about the validity of the various assumptions discussed earlier are presented in Section 3. New methodologies and techniques accounting for the errors associated with conventional indentation of isotropic linearly elastic solids are described in Section 4. The composite correction factor that involves finite tip radius and compressibility of the specimen is presented in close form, and the significance of each factor will be discussed in detail. Results from nanoindentation experiments on a nominally elastic solid (natural latex) are used to illustrate the application of the suggested techniques for accurate evaluation of material properties. A summary and conclusions of the study are presented in Section 5.

2. Conventional extraction of elastic properties

Assuming a linearly elastic half-space and rigid conical indenter, Sneddon (1948) found that

$$P = \frac{2E\tan\alpha}{\pi(1-\nu^2)}h^2 \tag{1}$$

where P is the load measured by the indenter, E and ν are the Young's modulus and Poisson's ratio of the material that is being indented, α is the half angle of the indenter, and h is the displacement of the indenter. While the validity of Sneddon's solution is limited to linearly elastic indentations, (1) is nonetheless routinely applied to elastic–plastic indentations by assuming that the initial unloading segment of the load–displacement curve is linearly elastic. In an elastic indentation where the loading and unloading curves follow the same path, (1) and subsequent derivations are valid at all h.

Differentiating (1) with respect to h, the slope of the load–displacement curve is given by

$$\frac{dP}{dh} = \frac{4E\tan\alpha}{\pi(1-\nu^2)}h \tag{2}$$

and with further algebraic manipulation (Fischer-Cripps, 2004)

$$\frac{dP}{dh} = \frac{2\sqrt{A}E}{\sqrt{\pi}(1-\nu^2)}, \tag{3}$$

where A is the projected area of contact of the indenter. Bulychev et al. (1975) showed that (3) also holds for cylindrical punch and spherical indenters. Subsequently, Pharr et al. (1992) showed that (3) is relevant for all axisymmetric indenters with infinitely differentiable profile. For a Berkovich/Vickers indenters, the angle $\alpha = 70.3°$, and the corresponding projected area, A is given by

$$A = \pi \tan^2 \alpha h_c^2 = 24.5 h_c^2, \tag{4}$$

where h_c refers to the contact depth (Fig. 1) and is given by (Fischer-Cripps, 2004)

$$h_c = h - \frac{2(\pi - 2)}{\pi} \frac{P}{dP/dh}. \tag{5}$$

Note that the coefficient of the second term on the right-hand side of (5) is often represented by a constant in literature, whose value is dependent on the geometry of the indenter (Pharr and Bolshakov, 2002).

Thus, using the load–displacement curve measured during an indentation, one can obtain the elastic constants of the specimen of interest using the following equation:

$$\frac{E}{(1 - \nu^2)} = \frac{1}{2\beta} \sqrt{\frac{\pi}{A}} \frac{dP}{dh}, \tag{6}$$

where β is a non-dimensional correction factor to account for deviations from the original stiffness equation ($\beta = 1$ in (6)). The factor β is used to account for the treatment of a pyramidal indenter as an equivalent conical indenter – β is unity for axisymmetric indenters and close to unity for pyramidal ones – $\beta = 1.012$ for square-based indenter, e.g., Vickers, and $\beta = 1.034$ for a triangular punch, e.g., Berkovich (King, 1987). However, these results are debatable as Woirgard (2006) demonstrated analytically that $\beta = 1.061$ and $\beta = 1.023$ for triangular and square-based indenters, respectively. Hay et al. (1999) considered the elastic radial displacement neglected in Sneddon's formulation and proposed a correction factor that is a function of the indenter's half angle, α and Poisson's ratio, ν. In addition, the correction factor β is also used to account for finite tip radius effect as found in the works of Troyon and Huang (2004). The deviation of a pyramidal indenter from a conical one is not relevant to this paper since only the conical indenter is considered. Furthermore, since the objective of this paper is to investigate the applicability of Sneddon's equation on nanoindentation, β is deliberately chosen to be one, so as not to introduce artificial effects into the analysis.

The right-hand side of (6) consists of terms that can be derived using the load–displacement measurements in an indentation experiment. Thus, using this relationship, the term on the left-hand side of the equation consisting of both E and ν, commonly referred to as the reduced modulus, E_r, can be evaluated. It is important to note that the elastic constants, E and ν evaluated using this procedure are coupled and thus require *a priori* knowledge of one of them to calculate the other. Also note that when the indenter is not considered as rigid, the reduced modulus, E_r is given by

$$\frac{1}{E_r} = \frac{(1 - \nu^2_{\text{specimen}})}{E_{\text{specimen}}} + \frac{(1 - \nu^2_{\text{indenter}})}{E_{\text{indenter}}}. \tag{7}$$

The load–displacement relationship derived by Sneddon (1948) assumed the specimen as a linearly elastic infinite half space and a conical indenter that is infinitely sharp. While these assumptions simplified the problem, it is important to note that it is virtually impossible to fulfill them in reality. In an experiment, the specimen to be tested is likely to have a finite geometry and so does the radius of curvature of the indenter. These deviations from the assumptions in deriving Sneddon's solution are inevitably transferred as errors to the derived elastic constants.

The goal of this paper is to identify the effects of the above-mentioned deviations from the assumptions used in Sneddon's derivation (1948), and quantify the error associated with the calculation of elastic constants using the conventional method

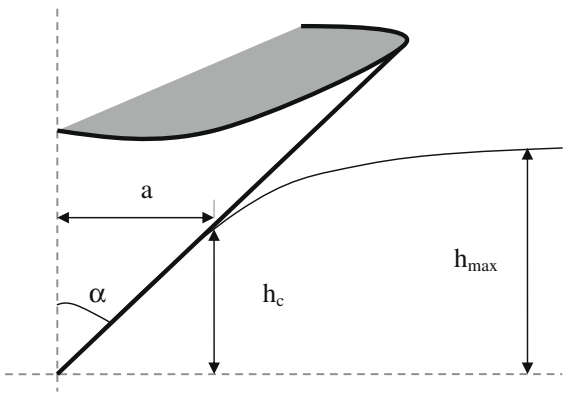

Fig. 1. Illustration of an indentation by a rigid cone into a linearly elastic solid.

proposed by Oliver and Pharr (1992). This paper considers a Berkovich equivalent conical indenter ($\alpha = 70.3°$) for which there is an available analytical solution (given by (1)). The elastic properties can be obtained using (6) with $\beta = 1$.

3. Numerical simulation

3.1. Sneddon's solution and a rigid indenter with finite tip radius

Numerical 'experiments' were performed using the commercial numerical finite element package, ABAQUS. A cylindrical specimen with a radius, r_s of 18 μm and a height, h_s of 30 μm, was indented on its top surface, along the axis of symmetry. The cylindrical specimen was modeled as an isotropic deformable solid with $E = 70$ GPa and $\nu = 0.3$. Fig. 2(a) is a three-dimensional illustration of the numerical simulation performed. The conical indenter was modeled as analytically rigid, with a finite tip radius, ρ of 200 nm, and was indented into the specimen to a maximum depth, h_{max} of 600 nm (displacement control). Details of the simulation will be included in the following section.

Fig. 2(b) shows a snapshot of the Mises equivalent stress field in the specimen when the indenter is at $h_{max} = 600$ nm. The region with highest stress is directly beneath the indenter tip. The boundary of the high stress region defined by the outlined area in Fig. 2(b) has an equivalent stress larger than or equal to 3.9 GPa. This region has a width of 2.1 μm and a maximum depth of 3.3 μm. This high stress region is located reasonably far away from the boundaries. The height and width of the area of high stress is close to 10 times smaller than that of the specimen and there is no visible interaction of the stress field with the boundaries of the specimen, which suggests that the specimen can be considered as sufficiently large for practical purposes.

The load (P) and displacement (h) curves from the numerical simulations are plotted in Fig. 3. The continuous solid curve refers to the load–displacement relationship for both the loading and unloading paths (elastic simulation – loading and unloading curves coincide) obtained from the simulation, while the dashed curve shows the load–displacement relationship derived from Sneddon, Eq. (1). It can be seen that the two curves are distinctly different. Using the conventional derivation described previously while assuming that the Poisson's ratio was known *a priori* to be 0.3, the Young's modulus was found to be 77 GPa, which is quite different from the value used in the simulation (70 GPa). This difference motivated the present study in order to first understand the effect of deviations from Sneddon's assumptions, and then to quantify and to correct for the errors associated with them, so as to obtain reliable values of the reduced modulus from experimental measurements.

3.2. Converged specimen geometry

It has been noted that the geometry of the specimen affects the values of measured load and displacement significantly (Dimitriadis et al., 2002). This is not surprising – consider two specimens loaded uniaxially (load control) with identical uniform stress and strain fields, the displacements of the specimens are not unique but functions of their geometries (i.e., length); this is also true for the measured load in a displacement control experiment.

Numerical simulations were performed to investigate the indentation problem, using the commercial finite element software, ABAQUS. The indentation experiment was modeled as a 2D axisymmetric problem using a total of 5006 three-node

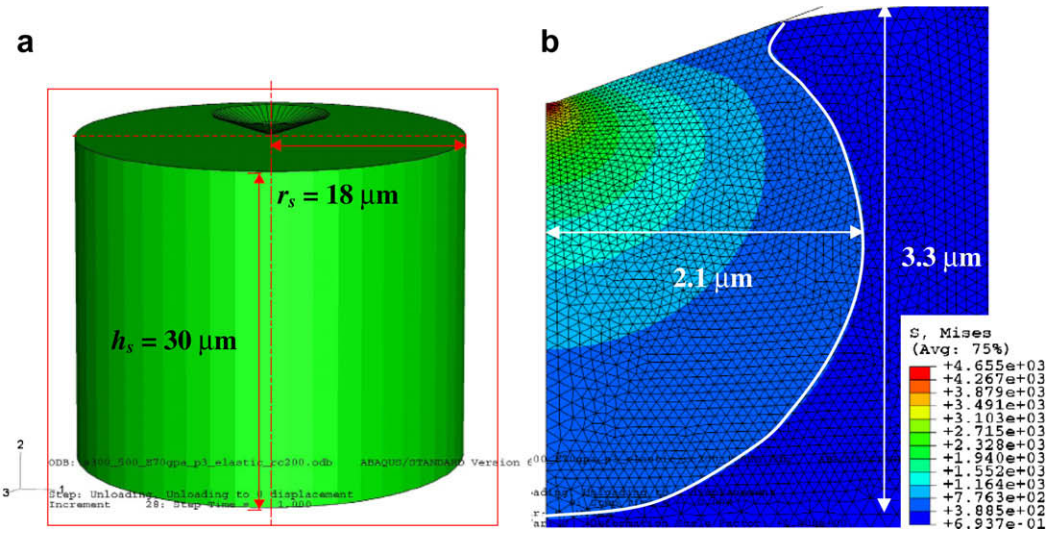

Fig. 2. (a) Geometry of indentation of a cylindrical specimen with a rigid conical indenter with finite tip radius. (b) The Mises equivalent stress field in the specimen during indentation at $h_{max} = 600$ nm. (Note that the stress values must be multiplied by a factor of 1×10^7 to respect the scale of the problem.)

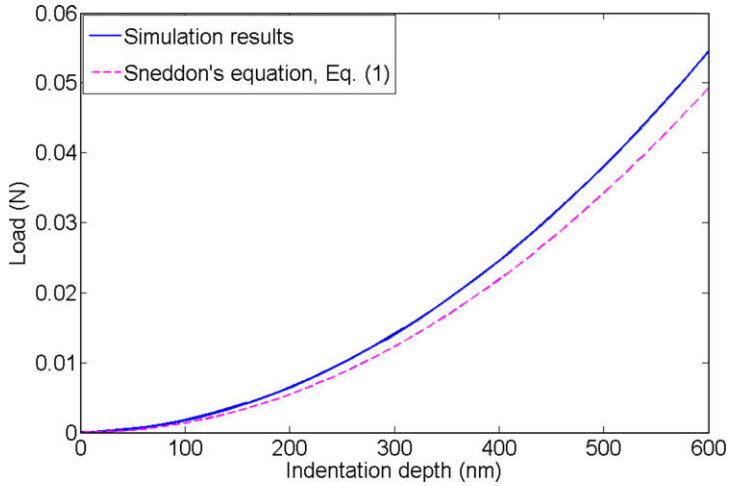

Fig. 3. Load–displacement measurements in the numerical experiment with a rigid indenter with a finite tip radius of 600 nm compared with Sneddon's equation (1).

linear axisymmetric triangular elements (CAX3) for a typically sized specimen whose dimensions are such that r_s/h_s equals unity and h_s/h_{max} equals 100 – the actual physical size of the specimen is irrelevant as the simulations are scaled to the indentation depth. The number of nodes used for individual specimens was scaled up and down for changes in their respective dimensions with respect to indentation depth. A more refined mesh by doubling the number of elements was used for each specimen size but did not yield significantly different results (<1% difference for the range of indentation depth of interest) for each simulation, which suggests convergence of the existing mesh. The mesh is denser at the indentation site and less dense away from the indentation to minimize computational time. In order to isolate the effects finite specimen size and finite tip radius of the indenters, the simulations were performed using conical indenters with the identical arbitrary tip radius; in addition friction was also excluded in the contact between the indenter and the specimen. The indenter was also pushed to a maximum indentation depth, h_{max} that is much larger than the radius of curvature of the tip, ρ in order to minimize any tip-geometry-transition effect – the conical tip is rounded off by a tangent sphere, whose radius gives the radius of curvature of the tip.

Elastic specimens with identical material constants (E = 70 GPa and ν = 0.3) and radius, r_s (18 μm) but different height, h_s (see Fig. 2(a)) were indented to the same maximum indentation depth, h_{max} (600 nm) in the numerical experiments performed. Fig. 4 shows the load–displacement relationship of each specimen recorded during the simulations (loading–unloading). It is observed that a thinner specimen will result in a higher load measurement for a given displacement or equivalently, at a given load, a smaller displacement. Despite having identical material properties, the specimens with different height, h_s

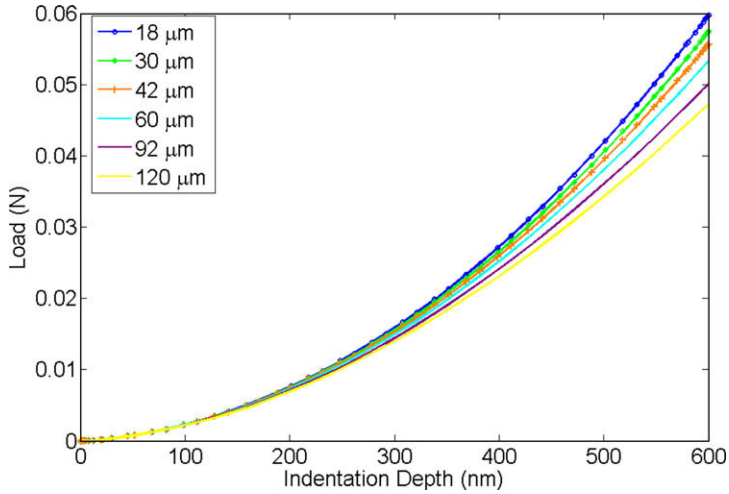

Fig. 4. Non-unique load–displacement relationships for specimens with the same radius, r_s of 18 μm but different heights, h_s (18, 30, 40, 60, 92, and 120 μm).

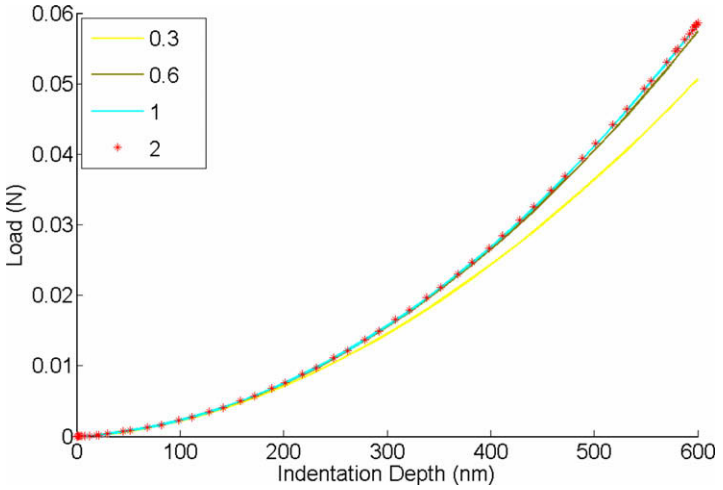

Fig. 5. Load–displacement curves for specimens with $r_s = 30$ μm and different aspect ratios, r_s/h_s (0.3, 0.6, 1, and 2). It can be observed that a unique curve was obtained when $r_s/h_s \geqslant 1$, suggesting convergence.

have distinctly different load–displacement curves. The first observation is that these differences will inevitably be passed on to the value of the reduced modulus evaluated using the conventional method discussed in the previous section. Dimitriadis et al. (2002) considered the problem of spherical indentation and corrected for the specimen thickness effect on the load–displacement relation.

Keeping h_s at 30 μm, the radius of the specimens, r_s was varied from 9 to 60 μm. The specimens were indented with the same indenter to the same maximum depth of 600 nm. From Fig. 5, it can be observed that the load–displacement curves converge when the aspect ratio, r_s/h_s equals or exceeds unity. The validity of converged aspect ratio was checked and confirmed for other values of h_s as well.

Specimens with converged aspect-ratio, but different h_s/h_{max}, were used in subsequent simulations to determine the minimum size of the specimens to achieve convergence. Fig. 6 plots their corresponding calculated load–displacement curves. It is observed that the load–displacement curves converge when the h_s/h_{max} equals or exceeds 100. From here on, converged specimen geometry will be defined as

$$r_s/h_s \geqslant 1$$

and

$$h_s/h_{max} \geqslant 100. \tag{8}$$

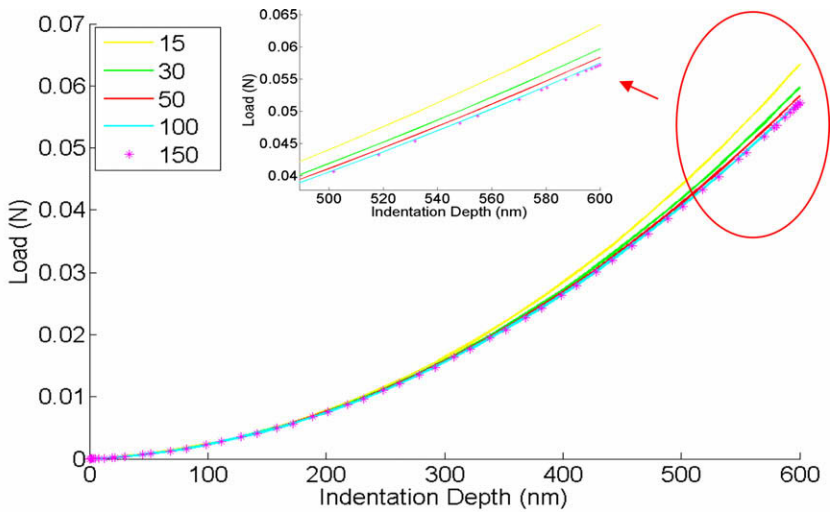

Fig. 6. Load–displacement curves for specimens with different h_s/h_{max}. Insert shows a close-up view of the load–displacement curves at larger indentation depths for different h_s/h_{max} (15, 30, 50, 100, and 150).

To save computation time, it is favorable to keep the specimen as small as possible, hence converged specimen geometry is defined as r_s/h_s equals unity and h_s/h_{max} equals 100.

There is a general 'rule of thumb' which suggests that convergence is achieved when h_s/h_{max} is larger than 10 (Fischer-Cripps, 2004). Fig. 2(b) shows that the depth of high stress region is about five times that of h_{max}, all of which may seem to suggest that (8) may be too stringent. However, as shown in Fig. 7, *both* criteria, shown in (8) have to be fulfilled in order to achieve convergence.

Fig. 7 shows an enlarged view of a segment of the load–displacement curves. As discussed previously, it is observed that for a given h_s/h_{max}, the curves converge when $r_s/h_s > 1$. It is also observed that for an 'unconverged' aspect-ratio, i.e. $r_s/h_s < 1$, convergence in the 'h_{max}/h_s sense' occurs much earlier. As seen in Fig. 7, for r_s/h_s of 1/2, the load–displacement curves for h_s/h_{max} of 25–150 coincide. However, one should note that this is a "pseudo-convergence" – a slight change in the aspect ratio of the specimen will result in a significant change in the load–displacement curves. This "pseudo-convergence" could occur for an even smaller h_s/h_{max} than 25, but not checked in this series of simulations, which could possibly explain why the conventional "rule of thumb" (which does not consider the aspect ratio) only requires $h_s/h_{max} > 10$. It is however, clear from the Fig. 7 that *both* $r_s/h_s > 1$ and $h_s/h_{max} > 100$, in order for convergence to be met.

3.3. Finite tip radius effect

When considering the geometry of the indenting cone, Sneddon assumed an infinitely sharp tip. In reality, the tip of the indenter has a finite tip radius of curvature. The finite tip radius effect was observed and explicitly discussed by many researchers over the years (Doerner and Nix, 1986; Shih et al., 1991; Wang et al., 2006; Yu et al., 2004). These authors generally perceived the finite tip radius effect as a deviation from the estimated projected tip area, A. Doerner and Nix (1986) calibrated the tip area function, $A(h_c)$ of the indenter using careful measurements from transmission electron microscopy (TEM) images (proposed by Pethica et al. (1983)). Shih et al. (1991) and Yu et al. (2004) corrected $A(h_c)$ by introducing a spherical cap on pyramidal equivalent conical indenters. Shih et al. varied the tip radius to fit the $A(h_c)$ measurements performed by Doerner and Pethica, while Yu et al., modified $A(h_c)$ such that it takes the function of a spherical indenter at shallow depth and that of a conical indenter when the indentation is deeper than the transition point, h_a, given by

$$h_a = \rho(1 - \sin\alpha), \tag{9}$$

where ρ is the tip radius of the indenter and α is the half angle of the cone. More recently, Wang et al. (2006) noted that using indenters with different tip radii resulted in significantly different load–displacement curves. The authors observed that the values of the measured load increase for a tip with a larger radius of curvature at the same indentation depth. They plotted the load–displacement curves for identical specimens using different tip radii and also tabulated some examples of the indenter's tip radius effect on the calculated Young's modulus, and discussed qualitatively some possible sources of error. This study will investigate quantitatively the effect of finite tip radius on the load–displacement curves of an elastic specimen.

The finite tip effect on load–displacement curves was observed in our simulations (Fig. 8), and it is consistent with the expectation that a blunt tip will require a greater load to penetrate the specimen to the same depth as compared to a sharp

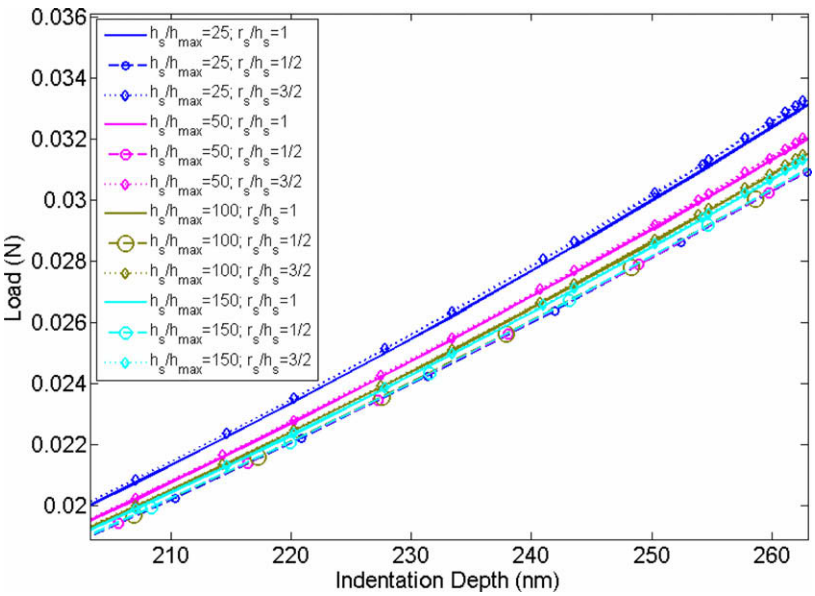

Fig. 7. Convergence study for different h_{max}/h_s and r_s/h_s.

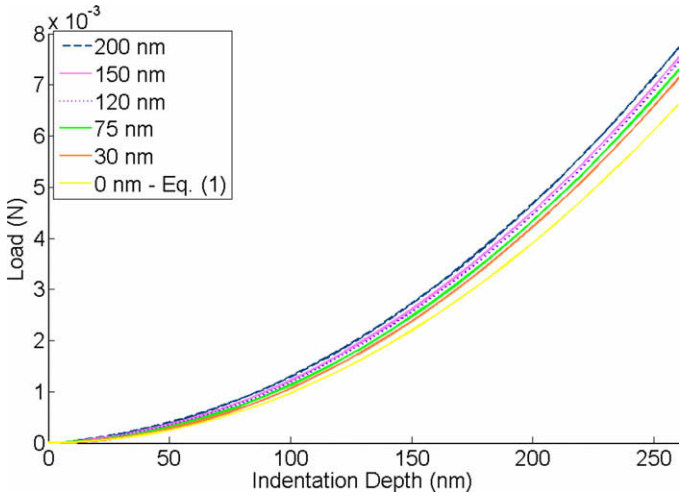

Fig. 8. Simulated load–displacement curves of identical elastic cylindrical specimens (E = 50 GPa, ν = 0.3) indented with rigid conical indenters of different tip radii, ρ (0, 30, 75, 120, 150, and 200 nm).

tip. It was noted that the correction for the finite tip radius effect is crucial for the accurate measurements of material properties especially in shallow indentations (Yu et al., 2004). To identify the effects of a finite tip radius, numerical simulations were performed. The conical tip used in the simulations was modeled to be analytically rigid, and had a tip radius of curvature that ranged from 30 nm to 1 μm. The cylindrical specimens used in the simulations had converged geometries as defined earlier (Eq. (8)). Their Young's moduli and Poisson's ratios ranged from 10 to 200 GPa, and from 0.01 to 0.49, respectively, in the simulations.

Unlike the load displacement relationship derived by Sneddon (Eq. (1)), where there is only an h^2 term, the load–displacement relationships obtained from these numerical 'experiments' were found to have the following form:

$$P = Kh(h + L), \tag{10}$$

where K and L are constant coefficients independent of P and h. The results from the simulations suggest that K is a function of the geometry of the indenter and the elastic constants of specimen similar to that in Sneddon's equation (Eq. (1)), while L is a function of the radius of curvature of the tip, ρ. A modified elastic indentation equation was derived empirically for the range of elastic properties and tip radii as mentioned previously

$$P = f(\nu)\frac{2E\tan(70.3^\circ)}{\pi(1-\nu^2)}h(h + g(\rho)) = (a_1\nu^2 + a_2\nu + a_3)\frac{2E\tan(70.3^\circ)}{\pi(1-\nu^2)}h(h + c_1\rho^2 + c_2\rho), \tag{11}$$

where, $a_1 = -0.062$, $a_2 = -0.156$, $a_3 = 1.12$, and $c_1 = 1.50 \times 10^4\ \mathrm{m}^{-1}$, and $c_2 = 1.17 \times 10^{-1}$.

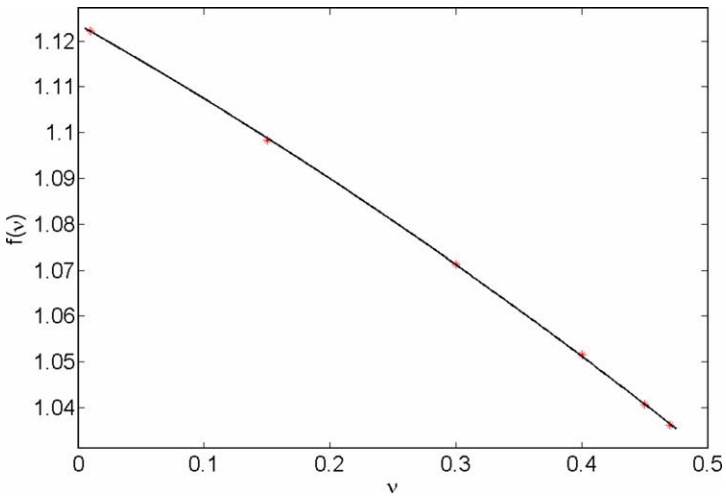

Fig. 9. Multiplicative factor, $f(\nu)$ as a function of Poisson's ratio, ν (R^2 = 0.9999).

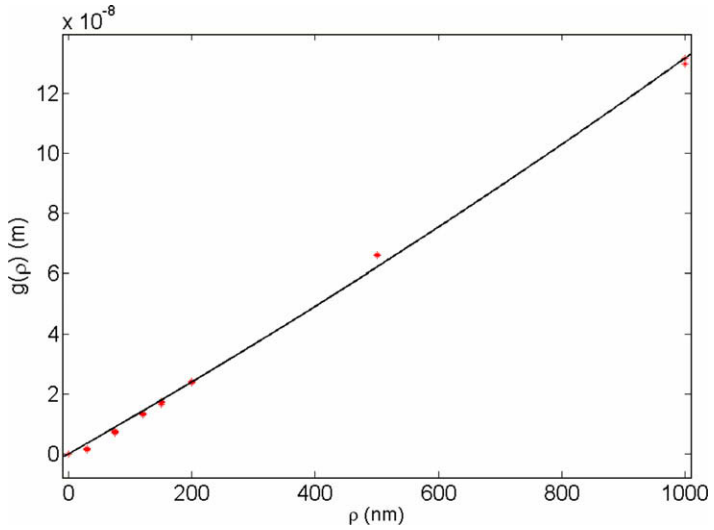

Fig. 10. Additive factor, $g(\rho)$ vs. tip radius, ρ (R^2 = 0.9977).

This equation fits the results from numerical simulation very well ($R^2 > 0.99$). For simple abbreviation, $f(\nu)$ and $g(\rho)$ are referred to as the multiplicative and additive factor, respectively. Figs. 9 and 10 shows the curve fit for the multiplicative and additive factor, respectively. It is interesting to note that there are two sources of divergence from the Sneddon's solution, namely both the multiplicative and additive terms. Sneddon's solution will be recovered when the multiplicative term equals one (unfortunately, when $\nu = 0.63$, which is physically unrealistic) and when the tip radius of curvature, ρ equals zero.

The multiplicative term, $f(\nu)$, similar to that found in the load–displacement relationship found empirically Larsson and Giannakopoulos (1996) for Berkovich indenters, is possibly due to the correction for radial displacements in Sneddon's solution when $\nu < 0.5$, as discussed by Hay et al. (1999).

Fig. 11 compares various correction factors, γ proposed by Hay et al. (1999), with $f(\nu)$ from (11) for a conical indenter with α of 70.3°. It can be observed that $f(\nu)$ in (11) is practically identical to the correction factor, $\gamma(\nu)$ proposed in Eq. (20) of (Hay et al., 1999) for ν smaller than 0.2. As ν approaches 0.5, this difference becomes larger. As compared to the functions proposed by Hay et al., $f(\nu)$ is observed to adequately describe the FEM results performed by Hay et al. at ν equals 0, 0.2, and 0.4. Unfortunately, however, there no FEM results were provided for comparison when ν approaches 0.5.

Fig. 12 shows the accurate description of (11), for elastic indentation of specimens over a range of elastic constants. The empirically derived load displacement relationship (Eq. (11)) matches the simulation results very well – the dotted lines represent Sneddon's analytical solution (Eq. (1)). With an accurate elastic load–displacement expression that includes the effect

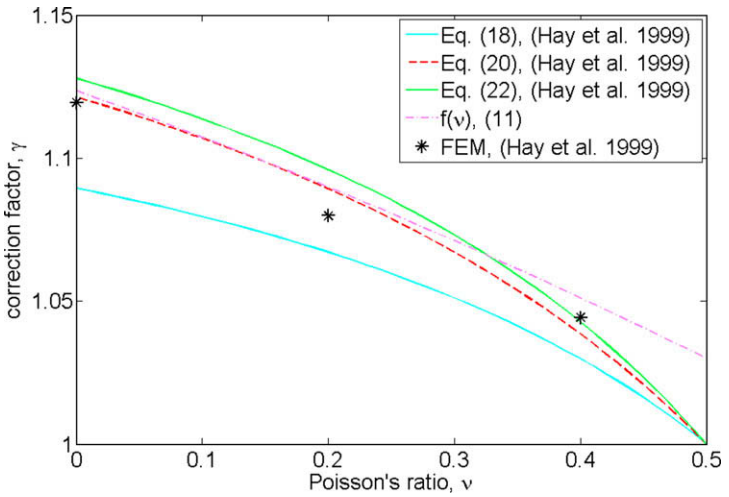

Fig. 11. Comparison of Hay's correction factor, γ and $f(\nu)$ (after Hay et al., 1999).

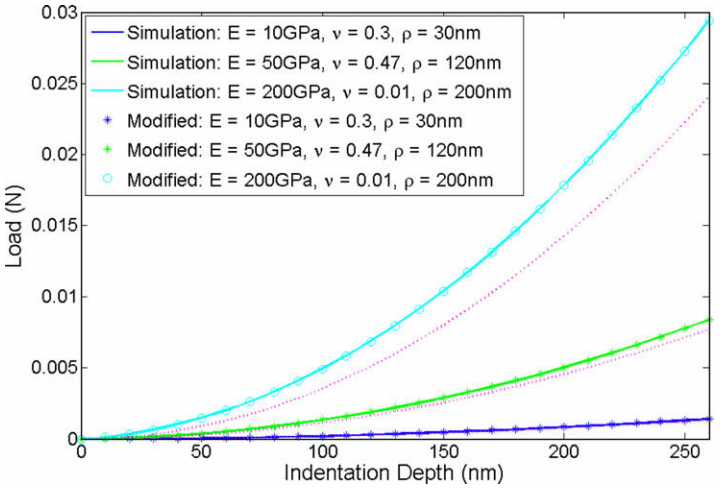

Fig. 12. Comparison of simulation results with proposed empirical curve fits for various material constants and tip radii of the rigid indenter.

of finite tip radius of the indenter, the elastic constants of an elastic specimen of interest can be derived in a straightforward manner. In the spirit of (6), the unknown elastic constants can be expressed as

$$\frac{E}{1-\nu^2}(a_1\nu^2+a_2\nu+a_3)=\frac{\pi\cot(70.3^\circ)}{2(2h+c_1\rho^2+c_2\rho)}\frac{\mathrm{d}P}{\mathrm{d}h}. \tag{12}$$

It is important to note that (11) can be used directly to solve for the elastic constants. It is not necessary to use the slope of the load–displacement curve, $\mathrm{d}P/\mathrm{d}h$, instead of the direct use of load–displacement measurement. The latter is in fact favorable due to the elimination of uncertainties associated with the measurement of the slope. However, (12) is used in subsequent parts of the paper to provide a direct comparison of the proposed load–displacement relationship with the existing one (6).

The first observation in examining (12) is that, similar to the conventional derivation, Young's modulus, E and Poisson's ratio, ν of the specimen are coupled. The second observation is that the coupled elastic terms on the left-hand side of the equation can be solved in a straightforward manner, provided the terms on the right-hand side are known. Thus, the following section proposes viable procedures to identify ρ using a calibration specimen, and to decouple the elastic constants, E and ν.

4. Proposed techniques and modifications

4.1. Technique for characterizing the tip radius of the indenter

The radius of the tips of nanoindenters are usually in the range of 50–200 nm, and it is often difficult to measure it accurately – the manufacturer can generally provide the radius of curvature of the indenters up to an uncertainty of 100 nm. There have been some suggested methods of retrieving the tip radius of the indenter. Shih et al. (1991) were able to retrieve the tip radius of the indenter by comparing the $A(h_c)$ of his proposed spherical cap model with that measured experimentally using TEM images, as described by Doerner and Nix (1986). Using the measured tip radius, Shih showed that there was good agreement between the results from numerical simulations and experiments. This method, however, is cumbersome to perform, and it is likely to fail for shallow indentations as it does not consider elastic recovery of the plastic imprint. Yu et al. (2004) proposed a method to retrieve the tip radius that is suitable for shallow indentations, by measuring h_a, using a "biocular spherical-conical" fitting method. This method however, is difficult to implement when α is large, as is the case for Berkovich/Vickers equivalent conical indenters. The large value of α will result in a small h_a (shown by (9)), thus making it difficult to accurately distinguish the spherical section from the conical one, using a least squares fit of this model. The procedure proposed here is suitable for large angle conical indenters ($\alpha = 70.3^\circ$) and does not require cumbersome measurements of the tip area function, $A(h_c)$ to retrieve the value of the tip radius.

The following example demonstrates how the tip radius of the indenter can be inferred in principle. The practicality of this technique is, however severely limited by the availability of a linearly elastic material. Suppose there is a'sufficiently large' (with converged geometry) linearly elastic specimen with $E = 50$ GPa and $\nu = 0.47$, indented by a rigid Berkovich/Vickers equivalent conical indenter with an unknown ρ to a maximum depth of 263 nm. The measured load–displacement curve is shown in Fig. 12.

The measured load–displacement curve is fitted with a quadratic curve using least square fit. The equation of the fitted curve is found to be

$$P = 1.182 \times 10^{11} h^2 + 1597h. \tag{13}$$

From (11), it can be shown that

$$c_1\rho^2 + c_2\rho = 1597/1.182 \times 10^{11}. \tag{14}$$

Solving (14), one obtains the following two roots for the equation:

$$\rho_1 = -7.90\ \mu\text{m} \quad \text{and } \rho_2 = 0.114\ \mu\text{m}.$$

It can be noted immediately that ρ_1 is inadmissible. One can confidently conclude that ρ = 114 nm, in this case. The indenter used in the simulation has a radius of curvature, ρ of 120 nm, which confirms that this procedure yields fairly accurate results within 5% of the true value. It should be noted that this method does not require a specimen with known material properties. However, the curve fitting process can be optimized over one variable (the coefficient of the h term), instead of two (the coefficient of the h^2 term is a function of E and ν), if the material properties of the specimen is known.

4.2. Methodology for decoupled measurements of linearly elastic constants, E and ν

An interesting observation is that the coupled elastic constants (E and ν) can be decoupled if two different indenters are used, of course, assuming that the specimen of interest is linearly elastic, which may be hard to come by. The load–displacement relationship for an elastic indentation using a spherical indenter is given by the Hertz equation (1881)

$$P = \frac{4}{3}\frac{E}{1-\nu^2}\sqrt{R}h^{3/2}. \tag{15}$$

Since there is no issue with finite tip radius in the case of spherical indenters, the simulated load–displacement curve is expected to coincide with Hertz equation. This was validated as shown in Fig. 13. As discussed previously, (6) is valid for all bodies of revolution, thus can be used in the case of spherical indenters. The tip area function of a spherical indenter (Fischer-Cripps, 2004) is

$$A_{\text{sphere}} \approx 2\pi R h_c, \tag{16}$$

where R is the radius of the spherical indenter and h_c is the contact depth. For an indentation with a spherical indenter, h_c is given by

$$h_c = h/2. \tag{17}$$

Fig. 13 illustrates two load–displacement curves corresponding to spherical and conical indenters, respectively. The spherical indenter has a radius, R of 400 nm and the specimen was indented to a maximum indentation depth, $h_{\max}$ of 150 nm. At $h_{\max}$, the slope was found to be 2.67×10^4 N/m, and the projected tip area of contact was found to be 1.86×10^{-13} m^2. Using (6), E_r was found to be

$$E_r = \frac{E}{1-\nu^2} = 54.8\ \text{GPa} \tag{18}$$

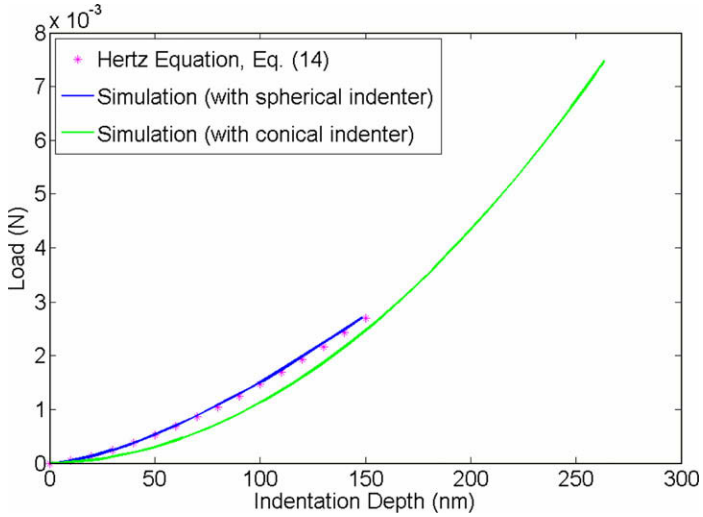

Fig. 13. Load–displacement curves for Hertz equation (Eq. (15)) and simulated indentations using spherical and conical indenters on identical specimens.

The conical indenter has a tip radius, ρ of 75 nm the specimen was indented to a maximum depth, h_{max} of 263 nm. At h_{max}, the slope was found to be 5.6×10^4 N/m. Using (12)

$$\frac{E}{1-\nu^2}(a_1\nu^2 + a_2\nu + a_3) = 58.9 \text{ GPa}, \tag{19}$$

where a_i are constants as defined in (11). Solving (18) and (19), Young's modulus, E, and Poisson's ratio, ν, were found to be 50.5 GPa and 0.281, respectively. The specimen was modeled with E = 50 GPa and ν = 0.3. This procedure does not require *a priori* knowledge of one elastic constant to derive the other, and instead it allows both the elastic constants to be calculated independently and simultaneously.

4.3. Quantifying error due to finite tip radius

Fig. 12 shows that (11) accurately describes the load–displacement measurements of elastic indentations using indenter with finite tip radius, and there are visible differences with the equation derived by Sneddon (Eq. (1)). It is of interest to quantify the error that is propagated in the derivation of elastic constants due to finite tip radius.

Since it was shown that the load–displacement relationship (using an indenter with a finite tip radius) can be accurately described by (11), one can thus use this equation to calculate the reduced modulus, E_r in the conventional way (Eq. (6)) as described in the previous section. The value of E can be extracted from E_r but substituting a known value of ν. The slope of the load–displacement curve can be obtained by differentiating (11), to calculate the contact depth, h_c, and projected area of contact, A. Differentiating (11)

$$\frac{dP}{dh} = \frac{2E\tan(70.3^\circ)f(\nu)(2h + g(\rho))}{\pi(1-\nu^2)}. \tag{20}$$

Recall (4) and solving for h_c as defined in (5), at h_{max}:

$$A = 24.5h_c^2 = 24.5\frac{h_{max}^2((\pi-4)g(\rho) - 4h_{max})^2}{\pi^2(2h_{max} + g(\rho))^2}. \tag{21}$$

Thus, one arrives at

$$\frac{E_c}{E} = \frac{0.35809}{h_{max}}f(\nu)(2h_{max} + g(\rho))\tan(70.3^\circ)\sqrt{\frac{(2h_{max} + g(\rho))^2}{((\pi-4)g(\rho) - 4h_{max})^2}}, \tag{22}$$

where E_c is derived Young's modulus using the conventional method described in Section 2. The ratio would be one if Young's modulus derived using the conventional method were equal to actual Young's modulus, E. Note that, the right-hand side of (22) is essentially equal to the correction factor, β as discussed by researchers to derive an accurate value for Young's modulus with nanoindentation. The correction factor in this case, appears to be the product of the first correction factor term, $f(\nu)$ due to radial displacement (Hay et al., 1999) and a term essentially related to the finite tip effects (the rest of the equation). This confirms the proposition by Troyon and Huang (2004). Without an explicit demonstration, the authors proposed that the correction factor, α is the product of γ (to account for the radial inward displacements) and β (a form factor related to the geometry of the indenter). However, unlike the correction factor proposed by Troyon and Huang, the right-hand side of (22) is a function of indentation depth. Taking the limit as h_{max} tends to infinity

$$\lim_{h_{max}\to\infty}\frac{E_c}{E} = f(\nu). \tag{23}$$

For deep linearly elastic indentations, the only relevant correction factor is $f(\nu)$, which accounts for the radial inward displacements; the finite tip radius effects are absent.

The percentage error, ε, is defined as

$$\varepsilon = \left(\frac{E_c}{E} - 1\right) \times 100. \tag{24}$$

The percentage error is plotted as shown in Fig. 14 for a specimen with Poisson's ratio, ν of 0.3, which is indented to maximum depths, h_{max} of 100 and 300 nm, respectively. The percentage error, ε is positive for the entire range of ρ, which suggests that the conventional method will result in an overestimation of the actual E. This phenomenon was observed for the range of E, ν, ρ, and h_{max} used in the simulations.

When ρ is equal to zero, the error arises from the multiplicative term, $f(\nu)$, which is a function of the Poisson's ratio, ν. Thus, for specimens with different ν, the intercept would be different. As the tip radius becomes larger, the percentage error increases significantly, which is consistent with expectation. The slope of the ε versus ρ curve is found to be highly dependent on h_{max}. Consider the use of an indenter with a tip radius of 150 nm, when the material parameters were obtained at h_{max} of 300 nm, the conventional derivation will overestimate E by close to 12%; however when obtained at h_{max} of 100 nm, the overestimation would be more than 20%. This suggests that the overestimation of E is more pronounced in shallow indentations, which is consistent with (23) demonstrating that finite tip radius effects are irrelevant in deep indentations.

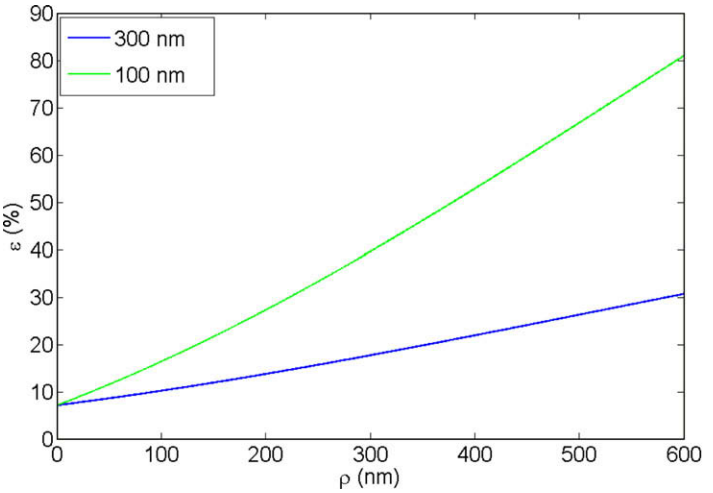

Fig. 14. Percentage error in estimation of Young's modulus, ε vs. tip radius, ρ for h_{max} = 100 and 300 nm.

It is important to note that these results were obtained in closed form through algebraic operations as described. The derivation does not take into account any surface and tip-geometry-transition effects, often associated with shallow indentations. This phenomenon is consistent with the observations by Yu et al. (2004), that the effect of "tip roundness" is more severe in shallow indentations.

4.4. Sensitivity the load–displacement measurements to finite tip radius effects

It has been shown that the finite tip radius effects cause the measured load–displacement curve to deviate from that derived by Sneddon (Eq. (1)). It is of interest to investigate the sensitivity of these effects.

Differentiate (11) with respect to ρ:

$$\frac{\partial P}{\partial \rho} = f(\nu)\frac{2E\tan\alpha}{\pi(1-\nu^2)}hg'(\rho). \tag{25}$$

The percentage change in measured load, ε_p, can be defined as

$$\varepsilon_p = \frac{\Delta P}{P} = \frac{g'(\rho)\Delta\rho}{h+g(\rho)}. \tag{26}$$

It is observed that at a given indentation depth, the percentage change in measured load is independent of material properties (E and ν). It should be noted that (26) is consistent with the previous discussion, showing that the deviation (in this case between measured load), measured with ε_p is more severe at shallow indentation.

For indentations using the nanoindenter, the tip radius is typically around 200 nm. Thus, considering a $\Delta\rho$ of 200 nm and solving around ρ of 200 nm and using (26), a minimum indentation depth of 467 nm is required, in order for the finite tip effects to be insignificant ($\varepsilon_p < 0.05$). Consider the typical load used in a nanoindentation to be around 10 mN, a material stiffer than 22 GPa will exhibit significant difference between an indentation with a infinitely sharp indenter and that with a finite tip radius of 200 nm.

The load–displacement measurement for an indentation on natural latex rubber is shown in Fig. 15. The experiment was performed using open loop load-control option on the Hysitron™ Triboindenter. The preload, P_o, required by the nanoindenter to establish contact, was set to be 2 μN. The indentation left no residual imprint.

The measured uniaxial stress–strain behavior of latex is shown in Fig. 16. It is observed that latex is essentially linearly elastic up to 10% strain. However, hysteresis can be observed in the load–displacement record suggesting the attainment of larger strains. To a first approximation, the average behavior of the material is considered as shown in Fig. 15.

The averages of the loading and unloading segments of several nanoindentations of natural latex are plotted in Fig. 17. Young's modulus, E of the latex was determined to be 3.46 MPa from uniaxial experiments, and its Poisson's ratio, ν was assumed to be 0.5. Using the values of P_o, E, and ν, load–displacement curves for the indentation were plotted for an infinitely sharp tip which corresponds to ρ of 0 nm, and for ρ of 200 and 400 nm, respectively. It is immediately observed that the effect of 200 nm in the tip radius of the indenter does not have such a significant effect on the load–displacement as that illustrated in Fig. 8. Using the average load–displacement curves from all the indentations performed, and assuming that the indenter tip is infinitely sharp, the Young's modulus for the latex indented was found to be 3.26 MPa, which is only about 6% error from the uniaxially measured Young's modulus. However, it is important to note the effects of preload in the indentation of soft materials. As illustrated in Fig. 17, the approximately 2 μN of load required for the load-cell to establish contact

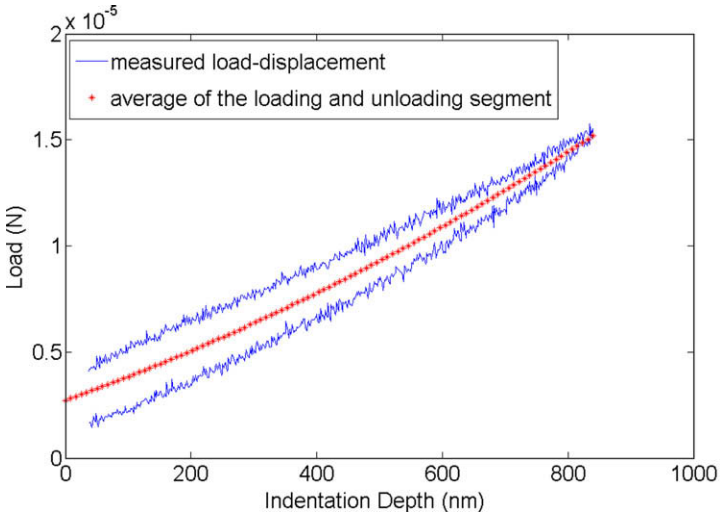

Fig. 15. Load–displacement measurement for the indentation of latex rubber.

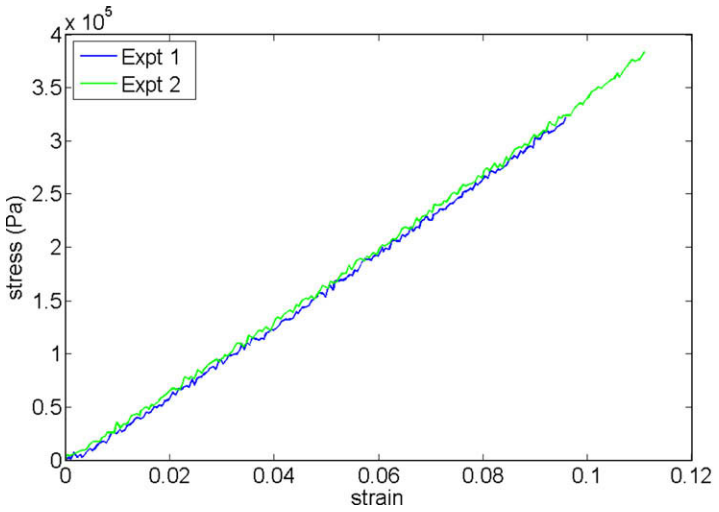

Fig. 16. Stress–strain relationship for natural latex from quasi-static uniaxial compression experiments.

results in about 500 nm of indentation depth in the specimen. This effect results in a shift of the non-linear load–displacement curve from the origin and if not accounted for, will be propagated into the stiffness measurement (slope of the load–displacement curve), resulting in a significant error in the derived reduced modulus.

As a final remark, the AFM is commonly used in the indentation of soft materials in the sub-μN force range. The tip radius for the AFM typically ranges from 10 to 60 nm. Despite the sharp tips used in these indentations, finite tip radius effects can become significant due to the low-load applied in the indentation, resulting in an indentation depth smaller than the critical for ε_p to be small. Consider $\Delta\rho$ of 20 nm and solving around ρ of 20 nm in (26), the minimum indentation depth, h_{crit} for ε_p to be less than 0.05, is 44.6 nm. Suppose the maximum indentation load is 1 μN, a material stiffer than 196 MPa, will result in ε_p larger than 0.05.

5. Summary and conclusions

The applicability of Sneddon's solution to the nanoindentation problem has been critically reassessed together with the implications of deviations from the basic assumptions in the analytical derivation, namely having:

1. a specimen with finite dimensions and
2. an indenter tip with a finite tip radius.

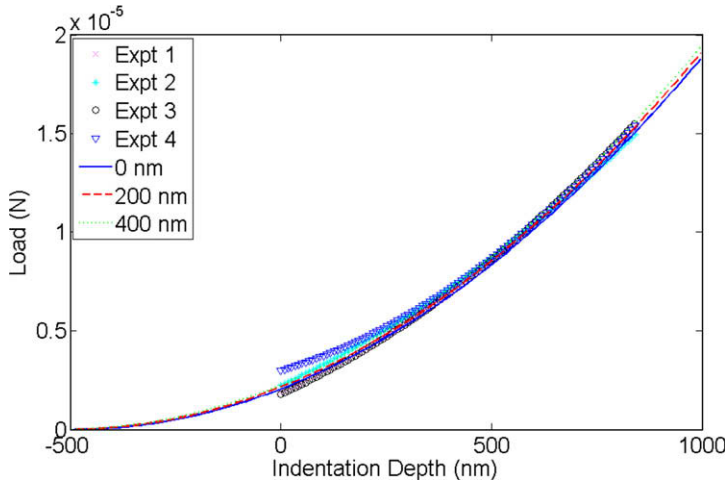

Fig. 17. Comparison of experimental results and predicted load–displacement relations for different ρ (0, 250, and 500 nm).

This study has clearly defined a criterion for "converged two-dimensional (axisymmetric) geometry" (Eq. (8)). Geometrical modeling issues are seldom detailed in the literature and this criterion will provide a common basis for comparison. In addition, this study addressed the finite tip effect and developed an accurate empirical load–displacement relationship that takes into account the finite tip radius, ρ (Eq. (11)). An estimate of the error arising from the neglect of the finite tip effect was provided by performing the conventional derivation procedure based on the load–displacement relation that takes the tip radius into account (Eq. (11)). It was found that the error consistently results in an overestimation of E (with known ν), which is more pronounced in shallow indentations. The error due to finite tip radius was also found to be more severe in shallow indentations. Finally, nanoindentation on natural latex was performed to experimentally examine the proposed model and techniques introduced in the paper.

Several aspects of nanoindentation have been explored in this work, namely:

1. A procedure to identify the indenter tip radius, ρ. The tip radius of the indenter is normally not provided by the manufacturers to a great accuracy, but it has been identified to be crucial for the accurate determination of elastic properties.
2. A procedure using two different indenters has been outlined to decouple the elastic constants, E and ν measured during indentation.

It should however be noted that the proposed procedures are limited to the availability of a linearly elastic material.

This work has shed light on several concepts related to the field of nanoindentation, but many open questions still remain. The ideas proposed in this paper are typically confined to indentations of linearly elastic solids. However, nanoindentation uses sharp indenters that are likely to induce plasticity on the very onset of loading. The validity of these observations in elastic–plastic indentations is addressed in an accompanying paper (Poon et al., 2008).

In conclusion:

- Sneddon's solution was modified to accommodate finite indenter tip radius.
- Valid two-dimensional specimen geometry for extracting the reduced modulus making use of the converged solutions must satisfy (8).
- The error associated with neglecting the finite indenter tip radius was quantified and an algebraic expression has been developed to account for this effect.
- For a known Poisson's ratio, ν, the error consistently results in an overestimation of the Young's modulus, E.
- The overestimation of E is more pronounced in shallow indentations.
- An experimental procedure to characterize the indenter's tip radius, ρ was proposed.
- An experimental procedure to decouple the measurement of the linearly elastic constants E (Young's modulus) and ν (Poisson's ratio) was outlined.

Acknowledgements

The research reported here was supported by the National Science Foundation (DMR # 0520565) through the Center for Science and Engineering of Materials (CSEM) at the California Institute of Technology is acknowledged. GR gratefully

acknowledges the Ronald and Maxine Linde Venture Fund that enabled the acquisition of the Hysitron™ Triboindenter used in this investigation. DR acknowledges the support of his visit to Caltech made possible through the Clark Millikan Visiting Professorship in Aeronautics.

References

ABAQUS. Hibbit, Karlsson & Sorensen, Inc., Pawtucket, RI.
Bhushan, B., Koinkar, V.N., 1994. Nanoindentation hardness measurements using atomic force microscopy. Appl. Phys. Lett. 64, 1653–1655.
Boussinesq, J., 1885. Applications des Potentials a l'Etude de l'Equilibre et du Mouvement des Solides Elastiques. Gauthier-Villars.
Bulychev, S.I., Alekhin, V.P., Shorshorov, M.K., Ternovskii, A.P., Shnyrev, G.D., 1975. Determining Young's modulus from the indentor penetration diagram. Zavodskaya Laboratoriya 41 (9), 1137–1140.
Chen, X., Ogasawara, N., Zhao, M., Chiba, N., 2007. On the uniqueness of measuring elastoplastic properties from indentation: the indistinguishable mystical materials. J. Mech. Phys. Solids 55, 1618–1660.
Cheng, Y.T., Cheng, C.M., 1999. Scaling relationships in conical indentation of elastic perfectly plastic solids. Int. J. Solids Struct. 36, 1231–1243.
Dao, M., Chollacoop, N., Vliet, K.J.V., Venkatesh, T.A., Suresh, S., 2001. Computational modeling of the forward and reverse problems in instrumented sharp indentation. Acta Mater. 49, 3899–3918.
Dimitriadis, E.K., Horkay, F., Maresca, J., Kachar, B., Chadwick, R.S., 2002. Determination of elastic moduli of thin layers of soft material using the atomic force microscope. Biophys. J. 82, 2798–2810.
Doerner, M.F., Nix, W.D., 1986. A method for interpreting the data from depth-sensing indentation instruments. J. Mater. Res. 1, 601–609.
Fischer-Cripps, A.C., 2004. Nanoindentation. Springer, Berlin.
Giannakopoulos, A.E., Larsson, P.L., Vestergaard, R., 1994. Analysis of vickers indentation. Int. J. Solids Struct. 31, 2679–2708.
Hay, J.C., Bolshakov, A., Pharr, G.M., 1999. A critical examination of the fundamental relations used in the analysis of nanoindentation data. J. Mater. Res. 14, 2296–2305.
Hertz, H., 1881. Uber Die Beruhrung Fester Elastischer Korper (on the contact of elastic solids). J. Reine Angew. Math., 156–171.
Hill, R., Storåkers, B., Zdunek, A.B., 1989. A theoretical study of the Brinell Hardness. Test. Proc. R. Soc. Lond. A 423, 301–330.
King, R.B., 1987. Elastic analysis of some punch problems for a layered medium. Int. J. Solids Struct. 23, 1657–1664.
Kral, E.R., Komvopoulos, K., Bogy, D.B., 1993. Elastic–plastic finite element analysis of repeated indentation of a half-space by a rigid sphere. J. Appl. Mech. 75, 829–841.
Larsson, P.L., Giannakopoulos, A.E., 1996. Analysis of Berkovich indentation. Int. J. Solids Struct. 33 (2), 221–248.
Laursen, T.A., Simo, J.C., 1992. A study of the mechanics of microindentation using finite elements. J. Mater. Res. 7, 616–618.
Lichinchi, M., Lenardi, C., Haupta, J., Vitalib, R., 1998. Simulation of Berkovich nanoindentation experiments on thin films using finite element method. Thin Solid Films 312, 240–248.
Loubet, J.L., Georges, J.M., Marchesini, O., Meille, G., 1984. Vickers indentation curves of magnesium oxide {MgO}. J. Tribol-T ASME 106, 43–48.
Newey, D., Wilkins, M.A., Pollock, H.M., 1982. An ultra-low-load penetration hardness tester. J. Phys. E: Sci. Instrum. 15, 119–122.
Oliver, W.C., Pharr, G.M., 1992. An improved technique for determining hardness and elastic modulus using load and displacement sensing indentation experiments. J. Mater. Res. 7, 1564–1583.
Pethica, J.B., Hutchings, R., Oliver, W.C., 1983. Hardness measurement at penetration depths as small as 20 Nm. Philos. Mag. A 48, 593–606.
Pharr, G.M., Bolshakov, A., 2002. Understanding nanoindentation unloading curves. J. Mater. Res. 17, 2660–2671.
Pharr, G.M., Oliver, W.C., Brotzen, F.R., 1992. On the generality of the relationship among contact stiffness, contact area, and the elastic modulus during indentation. J. Mater. Res. 7 (3), 613–617.
Poon, B., Rittel, D., Ravichandran, G., 2008. An analysis of nanoindentation in elasto-plastic solids. Int. J. Solids Struct. (submitted).
Shih, C.W., Yang, M., Li, J.C.M., 1991. Effect of tip radius on nanoindentation. J. Mater. Res. 6, 2623–2628.
Sneddon, I.N., 1948. Boussinesq's problem for a rigid cone. Proc. Cambridge Philos. Soc., 492–507.
Sneddon, I.N., 1965. The relation between load and penetration in the axisymmetric Boussinesq problem for a punch of arbitrary profile. Int. J. Eng. Sci. 3, 47–57.
Storåkers, B., Larsson, P.L., 1994. On Brinell and Boussinesq indentation of creeping solids. J. Mech. Phys. Solids 42, 307–332.
Ternovskii, A.P., Alekhin, V.P., Shorshorov, M.K., Khrushchov, M.M., Skvortsov, V.N., 1974. Micromechanical testing of materials by depression. Zavodskaya Laboratoriya 39 (10), 1242–1247.
Tranchida, D., Piccarolo, S., Loos, J., Alexeev, A., 2006. Accurately evaluating Young's modulus of polymers through nanoindentations: a phenomenological correction factor to Oliver and Pharr procedure. Appl. Phys. Lett. 89, 171905–171901-171903.
Troyon, M., Huang, L., 2004. Correction factor for contact area in nanoindentation measurements. J. Mater. Res. 30 (3), 610–617.
VanLandingham, M.R., Villarrubia, Guthrie, W.F., Meyers, G.F., 2001. Nanoindentation of polymers: an overview. In: Tsukruk, V.V., Spencer, N.D. (Eds.), Recent Advances in Scanning Probe Microscopy. Wiley, New York, pp. 15–43.
Wang, T.H., Fang, T.H., Lin, Y.C., 2006. A numerical study of factors affecting the characterization of nanoindentation on silicon. Mater. Sci. Eng. 447 (1–2), 244–253.
Woirgard, J., 2006. Some results on the indentation of an elastic half space. Philos. Mag. 86 (33–35), 5199–5217.
Yu, N., Polycarpou, A.A., Conry, T.F., 2004. Tip-radius effect in finite element modeling of sub-50 Nm shallow nanoindentation. Thin Solid Films 450, 295–303.